Supporting Information

Molecular insight in structure and activity of highly efficient, low-Ir Ir-Ni oxide catalysts for electrochemical water splitting (OER)

Tobias Reier[a]*, Zarina Pawolek[a], Serhiy Cherevko[b], Michael Bruns[c], Travis Jones[d], Detre Teschner[d], Sören Selve[e], Arno Bergmann[a], Hong Nhan Nong[a], Robert Schlögl[d], Karl J. J. Mayrhofer[b] and Peter Strasser[a]*

Experimental details (continued)

Substrates. Si wafers (<100>, B doped, Siegert Wafer) and Ti cylinders (Gemmel, grade 1, 10 mm diameter) were used as substrates for Ir-Ni mixed oxide thin-film preparation. Ti cylinders were grinded and polished consecutively to a mirror like surface finish using SiC grinding paper, diamond suspension (9 µm, Buehler) and silica suspension (0.02 µm, Buehler) in a half automatic polishing machine (AutoMet 250, Buehler). Thereafter, Ti cylinders were treated in hot nitric acid (23%, prepared by dilution of 69% HNO_3, AnalaR Normapur). Prior to spin coating all substrates were cleaned with ethanol and dried in nitrogen stream.

Electrochemical measurements. The MO-ap coated Ti cylinders were mounted into a custom made RDE sample holder made of polyetheretherketone (PEEK). The electrolyte, 0.1 M $HClO_4$, was prepared by dilution of 70% perchloric acid (Sigma-Aldrich, 99.999%) with ultrapure water (18 MΩ cm at room temperature).

Cyclic voltammetry was measured between 0.400 and 1.400 V_{RHE} consecutively with the following scan rates: 500, 200, 100, 50 and 20 mV s^{-1}. 100 cycles were performed at 500 mV s^{-1} to ensure a constant voltammogram, followed by 3 cycles at each following scan rate. Thereafter, the investigated voltage range was extended to reach from 0.050 to 1.400 V_{RHE} applying the same procedure as before.

Potential resolved inductively coupled plasma mass spectrometry (ICP-MS). During the measurement the electrolyte (0.1 M $HClO_4$) was pumped with a constant flow rate of *ca.* 180 µL min^{-1} through the flow cell and further downstream. The electrolyte was mixed with an internal standard in a Y-connector (mixing ratio 1:1) after the electrolyte has passed the flow cell and was then introduced into a Perkin Elmer NexION 300X ICP-MS. As internal standards for detection of ^{60}Ni and ^{193}Ir isotopes, 10 µg L^{-1} of ^{59}Co or ^{187}Re were used, respectively. For representative samples the measurement was repeated at randomly chosen fresh spots for at least three times. From these measurements an average error was determined which was then used as confidence range for every Ir dissolution measurement.

Selected area electron diffraction (SAED) sample preparation. The MO-ap films were scraped of the Si substrate with a scalpel and transferred to a carbon coated copper grid. Each sample was checked carefully for beam sensitivity during the SAED measurement.

X-ray diffraction (XRD). XRD profiles were measured in grazing incidence at 1° with Goebel mirror, Cu Kα source, a 0.23° secondary soller and scintillation counter as detector in a Bruker D8 Advance diffractometer (Bruker AXS). Data were collected with an increment of 0.05° and a measuring time of 40 s per step.

X-ray photoelectron spectroscopy (XPS). XPS measurements were performed using a K-Alpha XPS spectrometer (Thermo Fisher Scientific). All samples were analyzed using a microfocused, monochromated Al Kα X-ray source (30-400 µm spot size). The K-Alpha charge compensation system was employed during analysis, using electrons of 8 eV energy and low-energy argon ions to prevent any localized charge build-up. The analyzer transmission function, Scofield sensitivity factors,[S1] and effective attenuation lengths (EALs) for photoelectrons were applied for quantification. EALs were calculated using the standard TPP-2M formalism.[S2] The spectrometer was calibrated using the well-known photoelectron peaks of metallic Cu, Ag, and Au. According to the high conductivity of the samples no correction of the binding energy was applied. Sputter depth profiles were performed using a raster scanned Ar^+ ion beam (2x4 mm^2) at 1 keV and 30° angle of incidence. The sputter time required to reach the inflection point of the Ti (substrate) concentration was used as measure of the *film thickness* of the MO films. Accordingly, the *sputter depth (film thickness)*$^{-1}$ was determined as ratio of the actual sputter time and the sputter time assigned to the *film thickness*.

Density functional theory (DFT). All DFT calculations were performed using the Quantum ESPRESSO package[S3]. These were performed using the Perdew, Burke, and Ernzerhof exchange (PBE) and correlation potential[S4] with spin polarization and scalar relativistic corrections. Ultrasoft pseudopotentials from the PS library were employed with two Gauge Including Augmented Wave (GIPAW) projectors included for the l=1 channel of the oxygen pseudopotential for computation of the O K-edge spectra. Wave functions were expanded in a plane wave basis set with a kinetic energy cutoff of 50 Ry and a charge density cutoff of 500 Ry.[S5,6] An (8x8x8) **k**-point mesh was employed both for calculations using a unit cell equivalent to a 16 atom NiO cell and those using a 24 atom rutile IrO_2 cell, see Figures S7 and S9. Marzari-Vanderbilt cold smearing[S5] was used with a smearing parameter of 0.005 Ry to improve convergence.

To account for the on-site Coulomb interaction a simplified rotationally invariant method was used to include a Hubbard U on Ni. The value of 6.47 eV was computed by the linear response method of Cococcioni and de Gironcoli using a 16 atom cell of NiO with antiferromagnetic ordering along the [111] direction[S6]. While this value is higher than the 4.3 eV computed by Cococcioni and de Gironcoli using a norm conserving pseudopotential, the same value of U should not be expected as we employed a different pseudopotential. However, to ensure that our calculated U gives reasonable properties we compared the magnetic moment and optical gap to measured values. The magnetic moment per Ni atom computed with our U=6.47 eV is 1.8 μ_B, in agreement with the experimental value of 1.9 μ_B[S7]. Similarly, the optical gap in our calculation is ~2.9 eV around the *T* point, close to the value of 3.1 eV derived from optical absorption[S8] and the 2.7 eV[S6] and 2.8 eV[S9] from previous GGA+U and LDA+U calculations, respectively. And while the value of U depends on the nature of the chemical environment we found that it generally varied by only a few tenths of an eV in systems based on the 16 atom NiO cell. Thus, we employed a constant U of 6.47 eV in all calculations to allow the comparison of total energies.

Ion positions were allowed to relax until all components of the forces were less than 10^{-3} a.u. while the total change in energy was simultaneously less than 10^{-4} a.u. The cell volume and shape was also allowed to relax until the pressure vanished, within 0.5 kbar, after which an ionic relaxation was performed at fixed volume.

Core level binding energies (BE) were computed using the ΔSCF method to capture both initial and final state effects[S10]. In this method a relative core electron BE is computed by taking the difference in total

energy between a system with and without the relevant core hole included in the pseudopotential. For the O_{1s} the resultant relative binding energies were shifted to absolute binding energies using a reference calculation on a (4x4x4) supercell of IrO_2, for which we took the measured O_{1s} BE to be 530.1 eV.

The trace of the absorption cross section tensors used to generate the O K-edge spectra were computed from Fermi's golden rule with the continued fraction approach implemented in the XSpectra package[S11,12]. The cross sections of each symmetry unique absorbing atom were computed using an equivalent **k** point mesh to what was used to compute the charge density. To account for lifetime broadening the raw spectra were convoluted with a Lorentzian with an energy dependent linewidth: $\Gamma(E)=\Gamma_0+\Gamma(E)$. Γ_0 was taken as the natural linewidth of oxygen, 0.14 eV[S13]. $\Gamma(E)$ was assumed to increase linearly as $\Gamma(E)=0.1(E-E_{Fermi})$. This empirical change in linewidth has been shown to be reasonable for many systems[S14]. The Fermi energy of each computed spectrum was set to the computed O_{1s} BE of the absorbing atom to facilitate comparison with experimental results (except for the insulator NiO, where the computed O K-edge spectrum was aligned with experiment). The spectra of the pure oxides were well reproduced when the absorbing atom had no core hole in the pseudopotential, see Figures S6 and S8. As a result, we did not include an O_{1s} core hole when computing the O K-edge spectra of the mixed oxides.

The formation energy of the mixed oxides relative to NiO, IrO_2, O_2, and H_2 was computed as:

$$Eads = Etot - N_{Ni}\,E_{Ni} - N_{Ir}\,E_{Ir} - N_O\,E_O - N_H\,E_{H,} \qquad (1)$$

where $Etot$ is the total energy of the mixed oxide, N_x is the number of element x, where x= Ni, Ir, O, H, in the mixed oxide, and E_x is the energy of element x, which were taken as:

$$E_O = 1/2E_{O2}$$

$$E_{Ni} = E_{NiO} \quad 1/2E_{O2}$$

$$E_{Ir} = E_{IrO2} - E_{O2}$$

$$F_H = 1/2F_{H2}$$

The gas phase molecules were computed at the Γ point in a box with a side length of 40 bohr. Note that we chose to compute the formation energy relative to oxides as opposed to the pure metals to take advantage of error cancellation with the constant value U on Ni.

Figures

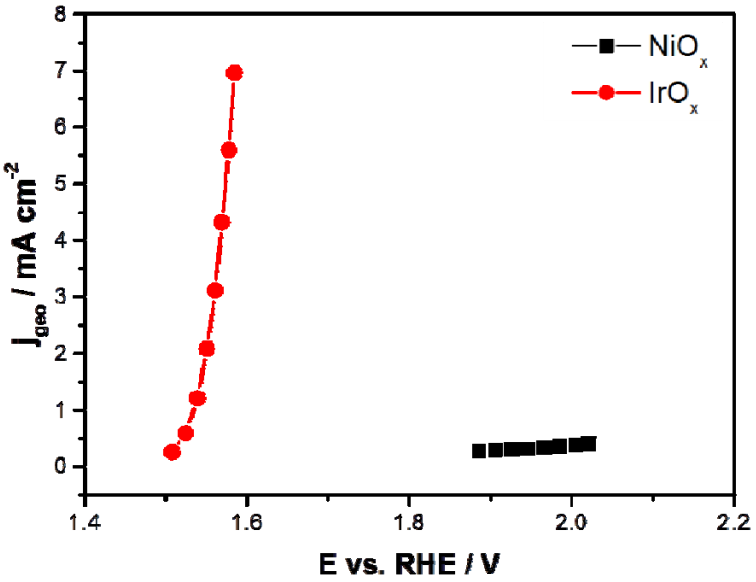

Figure S1: Quasi stationary polarization curves for pure Ir and pure Ni oxide films (iR corrected).

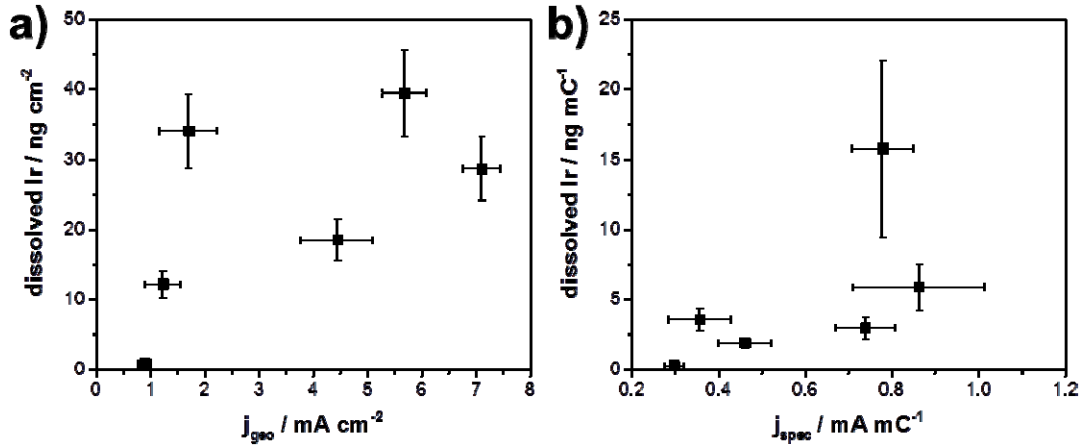

Figure S2: Comparative plots of the OER current density measured at 300 mV overpotential (1.530 V_{RHE}) and the amount of Ir dissolved during 30 min OER at 1 mA cm^{-2}. Current density and dissolved Ir amount were normalized to the investigated geometric surface area of the electrode (a) or, respectively, to q* (b).

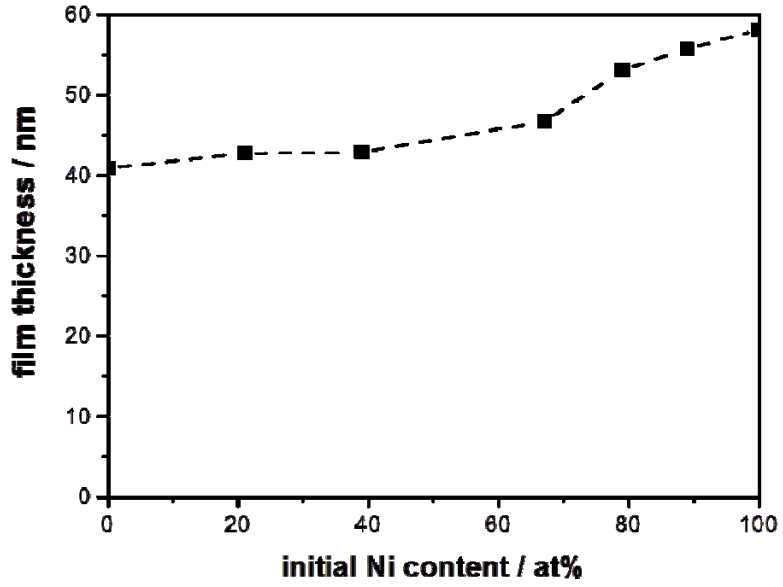

Figure S3: Film thickness of MO-ap as function of the initial Ni content measured by cross section SEM. Silicon wafers were applied as substrates.

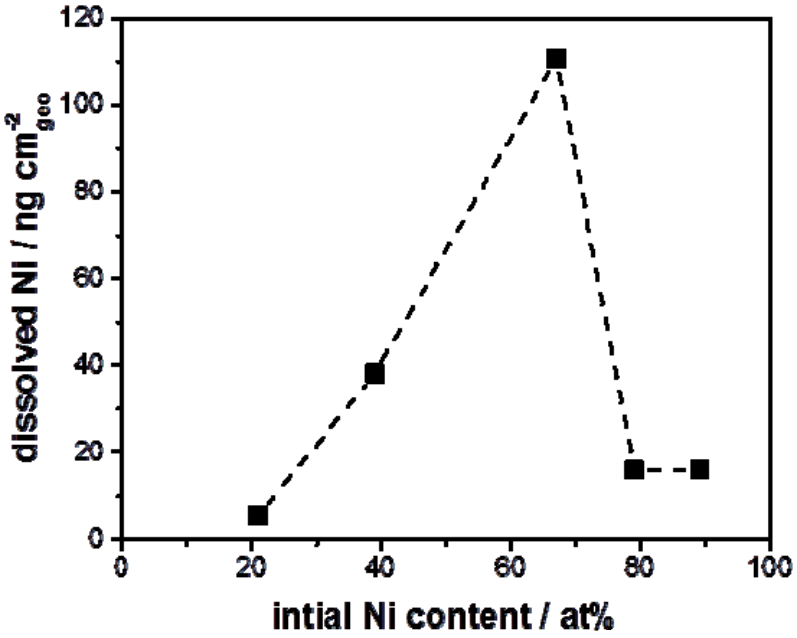

Figure S4: Amount of dissolved Ni during 30 min of OER at 1 mA cm^{-2} measured by potential resolved ICP-MS with MO-OER films.

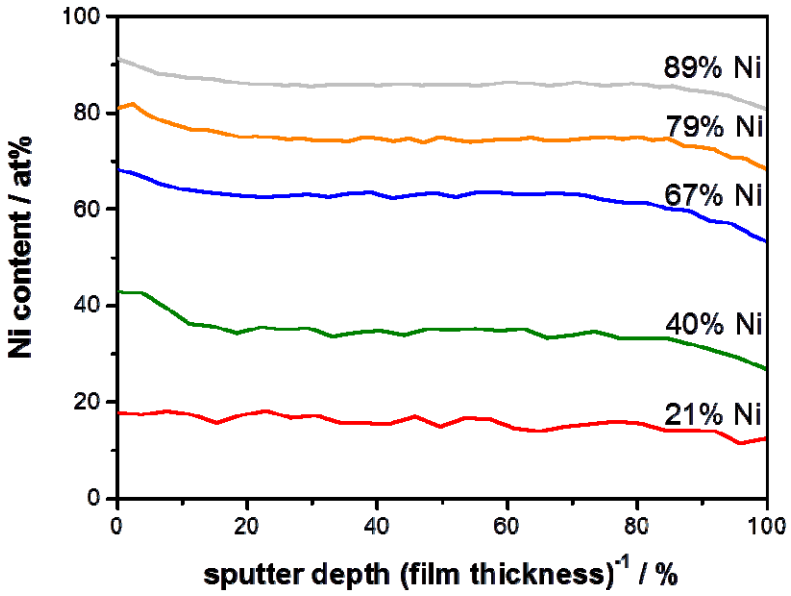

Figure S5: XPS sputter depth profile measurements for MO-ap.

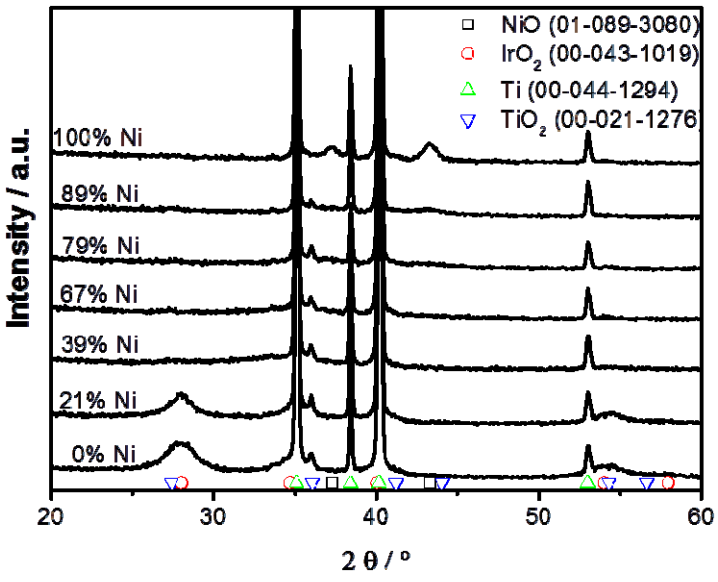

Figure S6: Grazing incidence X-ray diffraction measurements of MO-ap. References patterns from the powder diffraction file are provided for comparison.

X-ray absorption spectroscopy - DFT based theoretical treatment

NiO atomic and electronic structure

Figure S6 shows that the theoretical O K-edge spectrum computed for NiO is in good agreement with the measured spectrum.

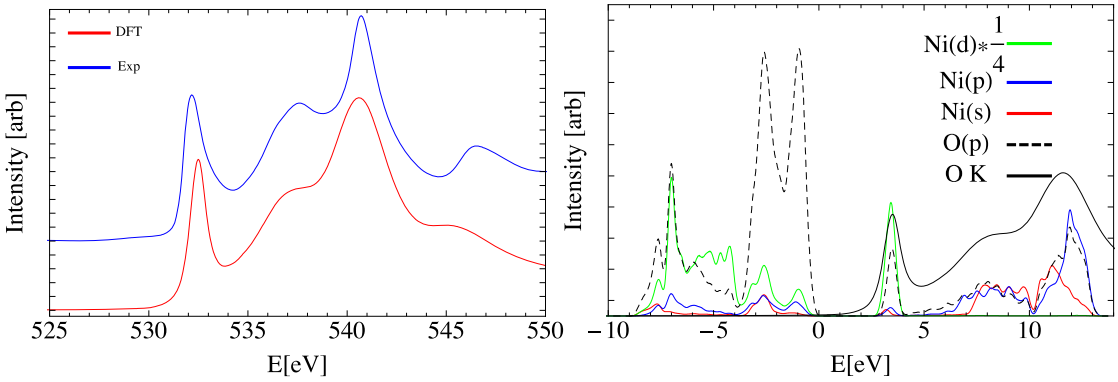

Figure S7: Comparison of the computed (red) and measured (blue) O K-edge spectra of NiO (left). PDOS of Ni-s, Ni-p, and Ni-d states together with the O-p states and the simulated O K-edge spectrum with the Fermi energy set to zero (right). The spin majority and minority components have been summed.

The projected density of states (PDOS) reveal that the feature at ~532 eV in the O K-edge spectrum is due to excitation into O-p states that mix with Ni-d states (Note that, as will be the case for all PDOS, the spin up and down components have been summed for simplicity). The features at excitation energies above ~532 eV are from transitions into O-p states that mix with Ni-p and Ni-s states, Figure S6 (right).

To aid in the identification of the nature of the 532 eV feature in the O K-edge spectrum, Figure S7 shows the atomic structure NiO together with the l-resolved Ni-d states and the O-p states. Because of octahedral symmetry, the oxygen states all transform together, while the Ni d-states are split into a doubly (d_{z2}, d_{x2-y2}) and triply degenerate (d_{xz}, d_{yz}, d_{xy}) e_g and t_{2g} pair. The oxygen states giving rise to the low energy feature in the O K-edge spectrum, at ~532 eV, mix only with the Ni (d_{z2}, d_{x2-y2}) orbitals, giving rise to nominally σ Ni-O anti-bonding states, as indicated by the orbital sketch in the upper right panel of the figure. There are no unoccupied Ni-O states that would be considered π anti-bonding, see the lower right panel of Figure S7.

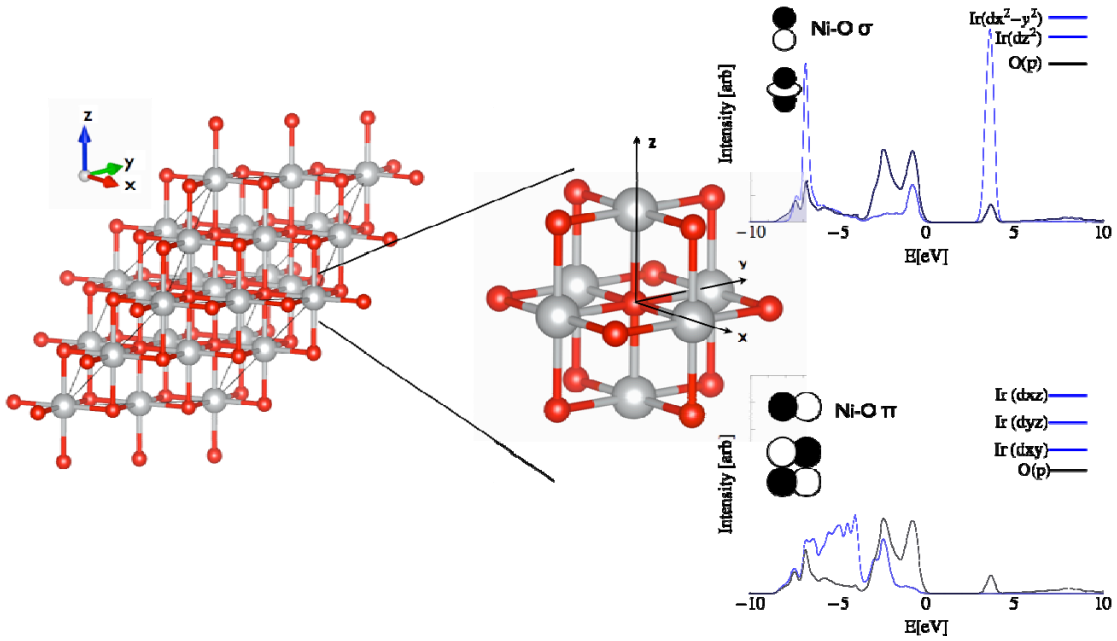

Figure S8: PDOS of l-resolved Ni-d states together with the O-p with the Fermi energy set to zero. The nickel atoms are shown as grey and the oxygen red. Orbital sketches are included on the PDOS plots to aid in visualization.

IrO_2 atomic and electronic structure

We found that the computed O K-edge spectrum of IrO_2 is also in good agreement with experiment, see Figure S8 (left). Here the O-p states giving rise to both the absorption signals at 530 and 534 eV are due to states hybridized with Ir-d states, see Figure S8 (right). The broad absorption starting signals at ~540 eV are due to excitation into O-p states hybridized with Ir s/p states.

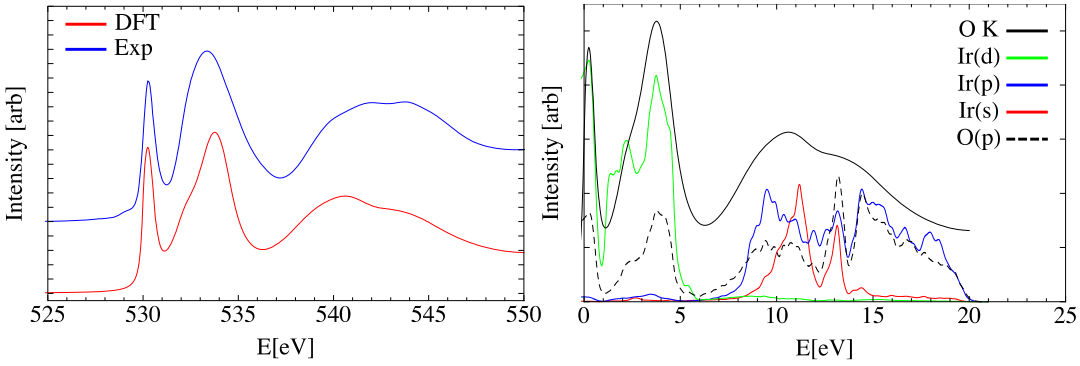

Figure S9: Comparison of the computed (red) and measured (blue) O K-edge spectra of IrO_2 (left). PDOS of Ir-s, Ir-p, and Ir-d states together with the O-p states and the simulated O K-edge spectrum with the Fermi energy set to zero (right).

The lower right panel of Figure S9 reveals that the absorption signal at ~530 eV is due to excitation into O-p states that are nominally Ir-O π anti-bonding. In the given coordinate system these states are the result of O-p_y mixing with the pair of Ir d orbitals, d_{xz} and d_{yz}. (Note that the Ir is not in a rigorous octahedral environment. Thus, the d_{xz} and d_{yz} states no longer transform together as part of the t_{2g} set, as discussed in Ref. [S15]. The upper right panel of Figure S9 shows that a second pair of orbitals, d_{z2} and d_{xy}, mix with the oxygen p states giving rise to the feature at 534 eV in the O K-edge spectrum, which are nominally σ Ir-O anti-bonding states. The d_{x2-y2} state on Ir can be seen to not effectively mix with unoccupied Op states. Thus, in contrast to NiO, the low energy part of O Kedge spectrum of IrO_2 is due to transitions into states that are nominally Ir-O π and Ir-O σ anti-bonding states.

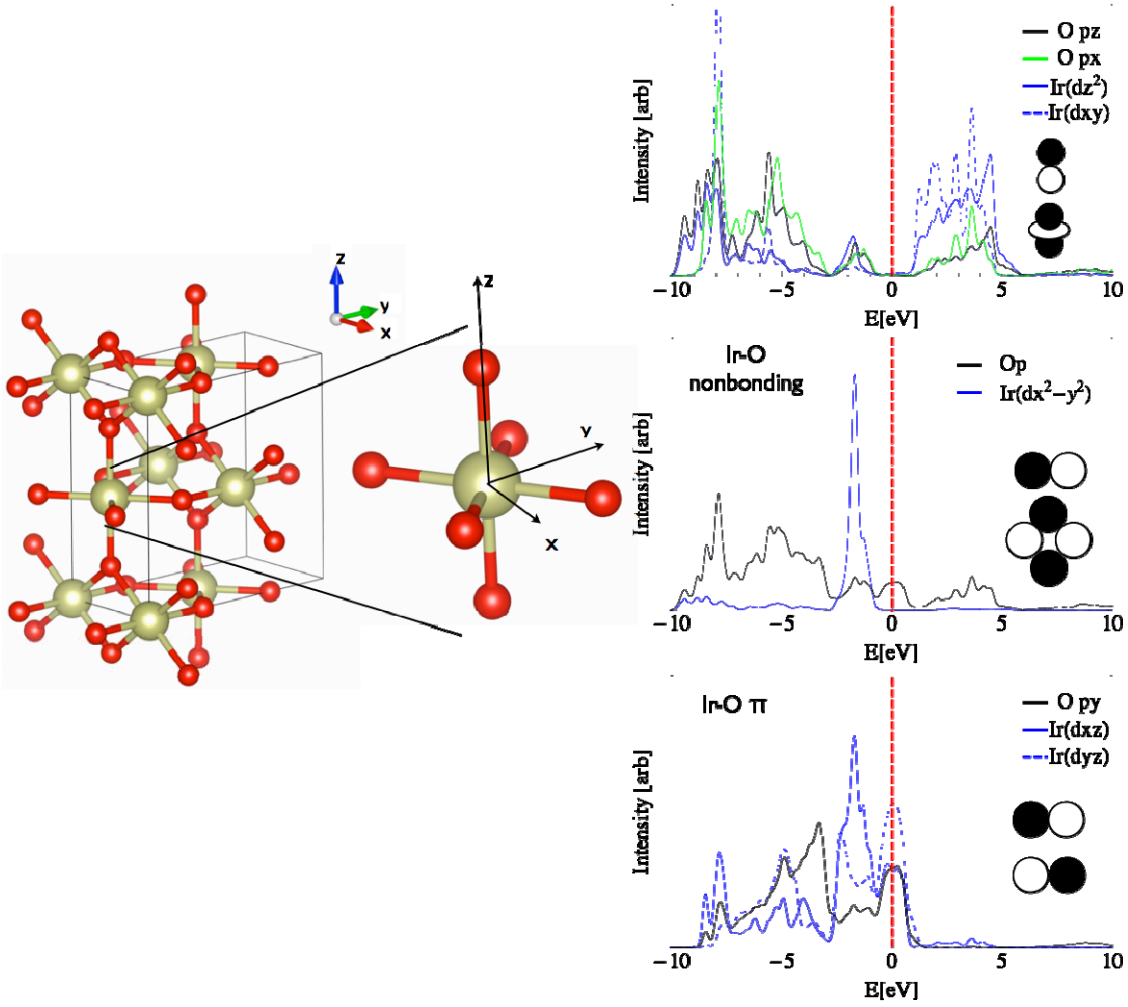

Figure S10: PDOS of l-resolved Ir-d and O-p states with the Fermi energy set to zero. Oxygen atoms are shown as red and the Ir as brown. Sketches of the orbital overlap are shown to aid in visualization.

21%Ni-MO-ap atomic and electronic structure

To model the 21%Ni-MO-ap we used Ir_7NiO_{16} in a rutile structure, that is, the Ir_8O_{16} with Ni substituted for one Ir, as shown in Figure S10, giving 13%Ni-MO. The Ni in this structure has a moment of 0.9 μ_B, while the remaining atoms have moments less than 0.1 μ_B. The formation of this mixed oxide relative to the pure oxides and O_2 is exothermic by 1 eV, as defined in Equation 1, significantly lower in energy than 86%Ni-MO. However, there are two types of oxygen atoms, those bound to Ir only and those coordinated by Ir and Ni. The simulated O K-edge spectra of each are shown in Figure S10, along with the total simulated O K-edge spectrum.

The O K-edge spectrum of O coordinated to Ir only is similar to that of IrO_2, while an excitation into O-p states on oxygen coordinated by Ir and Ni gives rise to the feature at ~529 eV in the total spectrum, see Figure S10. As with the previous mixed oxide, this low energy absorption is due to excitation into O-p states hybridized with Ir d states and Ni-d states. In this case, however, the number of Ni-d states involved in M-O π anti-bonding is larger than was observed in 89%Ni-MO (see below).

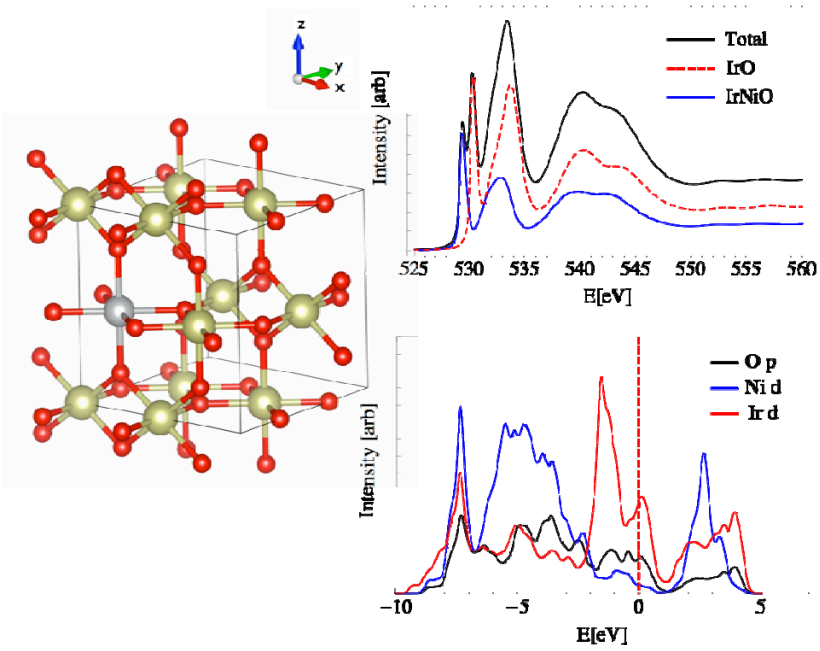

Figure S11: The structure and computed O K-edge spectrum and l-resolved PDOS on oxygen bound to Ni in the computed 13%Ni-MO. Oxygen atoms are shown as red, Ir as brown and Ni as grey.

89%Ni-MO-ap atomic and electronic structure

We modeled the Ir-Ni mixed oxide with 89% Ni content as Ni_6IrO_8, which is an 86%Ni-MO. The structure was selected by first substituting one Ni atom in the 16 atom NiO cell. The lowest energy structure retained was ferrimagnetic with opposing moments alternating on (111) planes with an average

moment on the Ni atoms of 1.6 μ_B and a 0.12 μ_B moment on the Ir atom. The low moment on the Ir atom leads to a total magnetization of 1.2 μ_B. By equation 1 the formation energy of this structure relative to the pure oxides and O_2 is +4 eV, that is, it is less thermodynamically stable than the phase separated oxides, though still significantly more stable than the bulk metals and O_2 gas. We found that introducing a Ni vacancy was exothermic by 3 eV, leading to the structure shown in Figure S11 and S12. This structure is also ferrimagnetic with opposed spins ordering along the [111] direction. The moment per Ni atom is 1.7 μ_B, slightly less than the 1.8 μ_B computed for NiO, while that on Ir is 0.5 μ_B, giving a total magnetization of 1.0 μ_B.

Inspection of Figures S11 and S12 reveals that Ni_6IrO_8 has two symmetry unique oxygen atoms, one type coordinated by only Ni and the second type coordinated by Ir and Ni. Thus, the O K-edge spectrum has contributions from two species. In each unit cell there are two oxygen atoms coordinated by Ni only, with the remaining six coordinated by both Ni and Ir. Taking these ratios, the total computed O K-edge spectrum of Ni_6IrO_8 can be seen to be in good agreement with experiment, see Figure 4d.

In Figure 4d the contributions from the O coordinated only by Ni and that coordinated by Ni and Ir are shown by way of the dotted and dashed black lines, respectively. As before, only the low energy features are associated with O-p states hybridized with metal d-states. While the simulated spectrum of oxygen coordinated by Ni alone is similar to that of NiO, a new feature appears in the total spectrum at 529 eV that is almost entirely due to transitions into O-p states on oxygen bound to both Ir and Ni. This type of oxygen also gives a doublet at 531, 533 eV, which appears as a single broad peak in the measured spectrum.

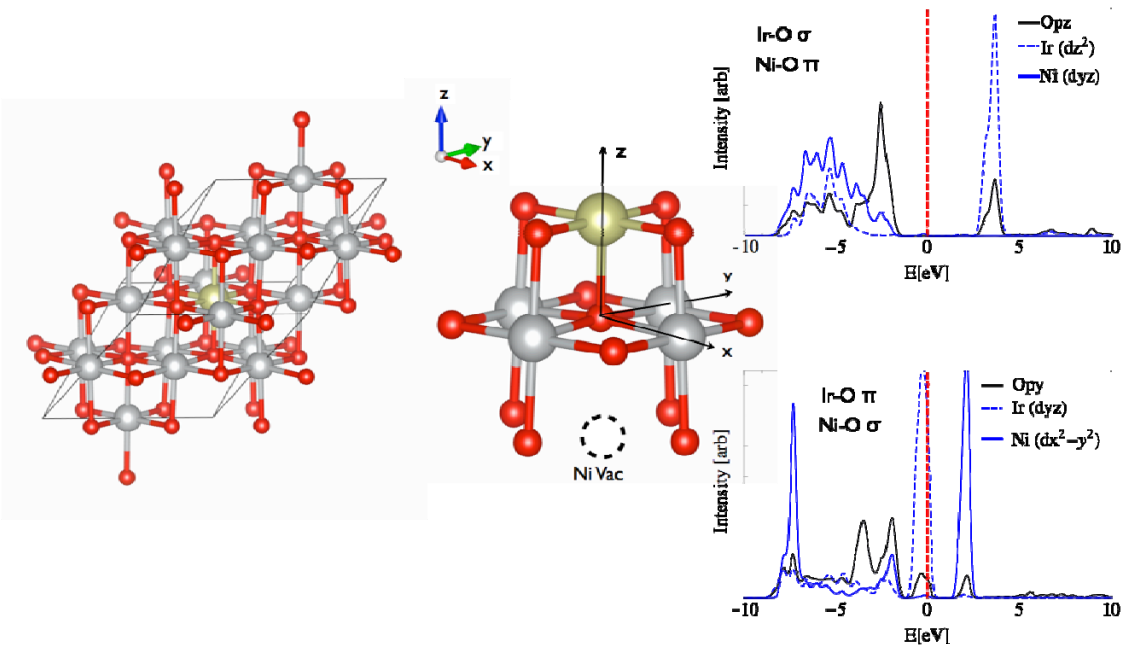

Figure S12: The l-resolved PDOS on oxygen coordinated by both Ni and Ir in the computed 86%Ni-MO-ap. The Ni atoms are shown as grey, the Ir as brown, and the oxygen as red.

The local structure around oxygen coordinated by Ir and Ni is shown in Figure S11, along with the l-resolved PDOS. Because both the Ni and Ir are octahedrally coordinated their d states transform as a doubly (d_{z2}, d_{x2-y2}) and triply degenerate (d_{xz}, d_{yz}, d_{xy}) e_g and t_{2g} pair. Inspection of the figure reveals that the feature at ~529 eV in the simulated O K-edge spectrum of this structure is due to O-p states hybridized with the Ir-d states transforming a t_{2g}, Ir-O π anti-bonding. O-p states involved in Ni-O σ and Ir-O σ anti-bonding states, that is, mixing with metal states transforming as e_g, can be seen to give rise to the features at 531 and 532 eV, respectively.

As may be expected, the O atom coordinated by Ni only has absorptions into Ni-O σ anti boding states, giving rise to the feature at 531 eV in the simulated O K-edge spectrum, see Figure S12. A second weak feature at ~529 eV may be due to the partial emptying of O states hybridized with Ni (d_{xz}, d_{yz}, d_{xy}) states, which are nominally Ni-O π anti-bonding. However, the contribution from these states is small.

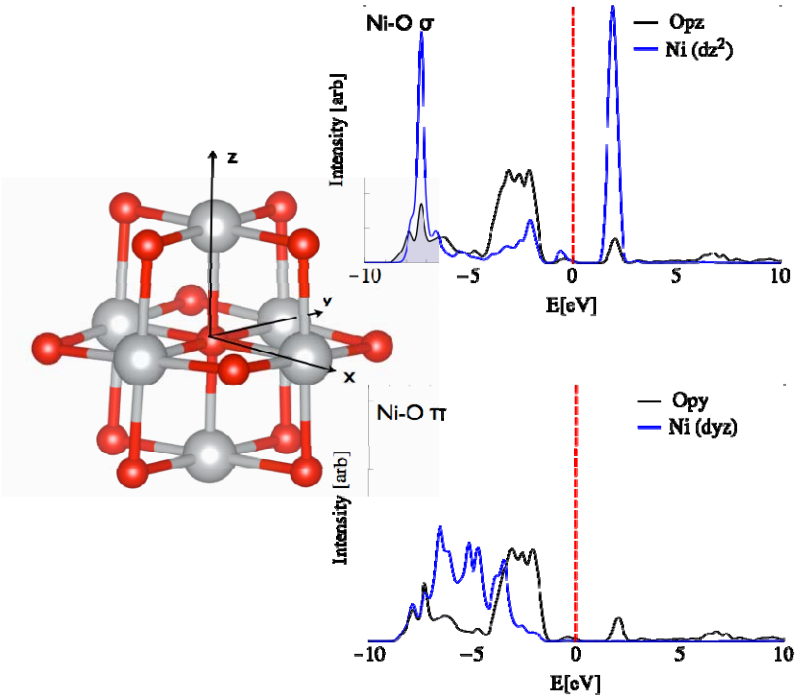

Figure S13: The l-resolved PDOS on oxygen bound to Ni in the computed 86%Ni-MO.

21%Ni-MO with H: atomic and electronic structure

As a final consideration we examined the hydrogenation of 13%Ni-MO, yielding $Ir_7NiO_{16}H_2$. The choice of adding 2 hydrogen atoms was made to maintain charge neutrality under the assumption that the formal oxidation states are Ir^{4+}, Ni^{2+}, and O^{2-}. Of the structures examined that shown in Figure S13 was of lowest energy, where the hydrogen atoms have attached to the oxygen atoms coordinated to both Ni and Ir, lowering the energy of the parent structure by 1.1 eV relative to Ir_7NiO_{16} and gas phase H_2, though the

atomic magnetic moments remained almost unchanged. Introducing the hydrogen atoms can be seen to diminish the absorption at 529 eV in the total simulated O K-edge spectrum and shift the feature at ~533 eV in the absence of H to ~534 eV.

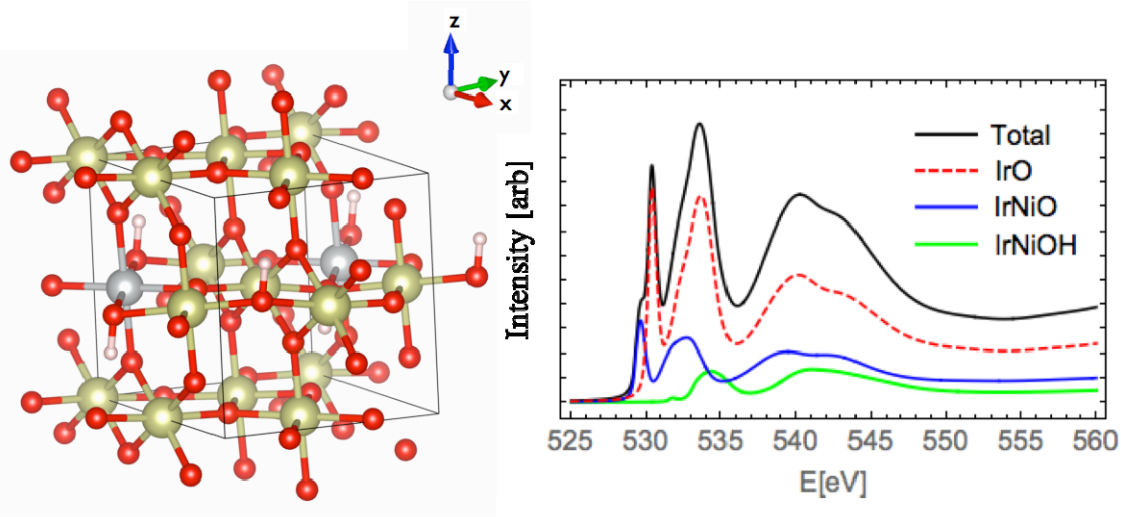

Figure S14: The structure and computed O K-edge spectrum of hydrogenated 13%Ni-MO. Oxygen atoms are shown as red, Ir as brown and Ni as grey.

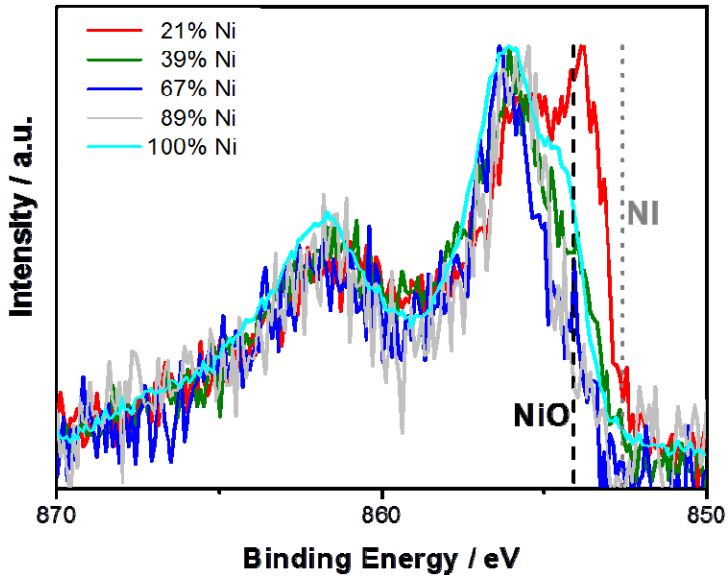

Figure S15: X-ray photoelectron spectra of the Ni 2p region of MO-OER provided together with reference binding energies for Ni[S16] and NiO[S17].

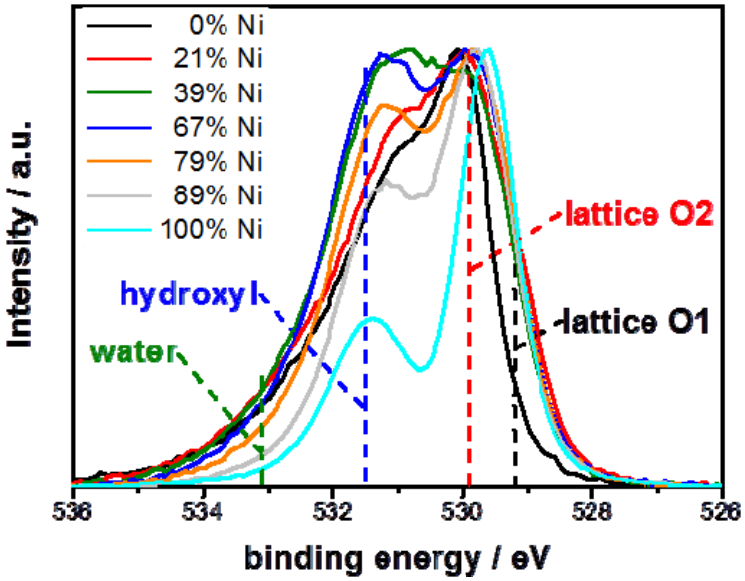

Figure S16: X-ray photoelectron spectra of the O1s region of MO-ap provided together with reference binding energies[S18].

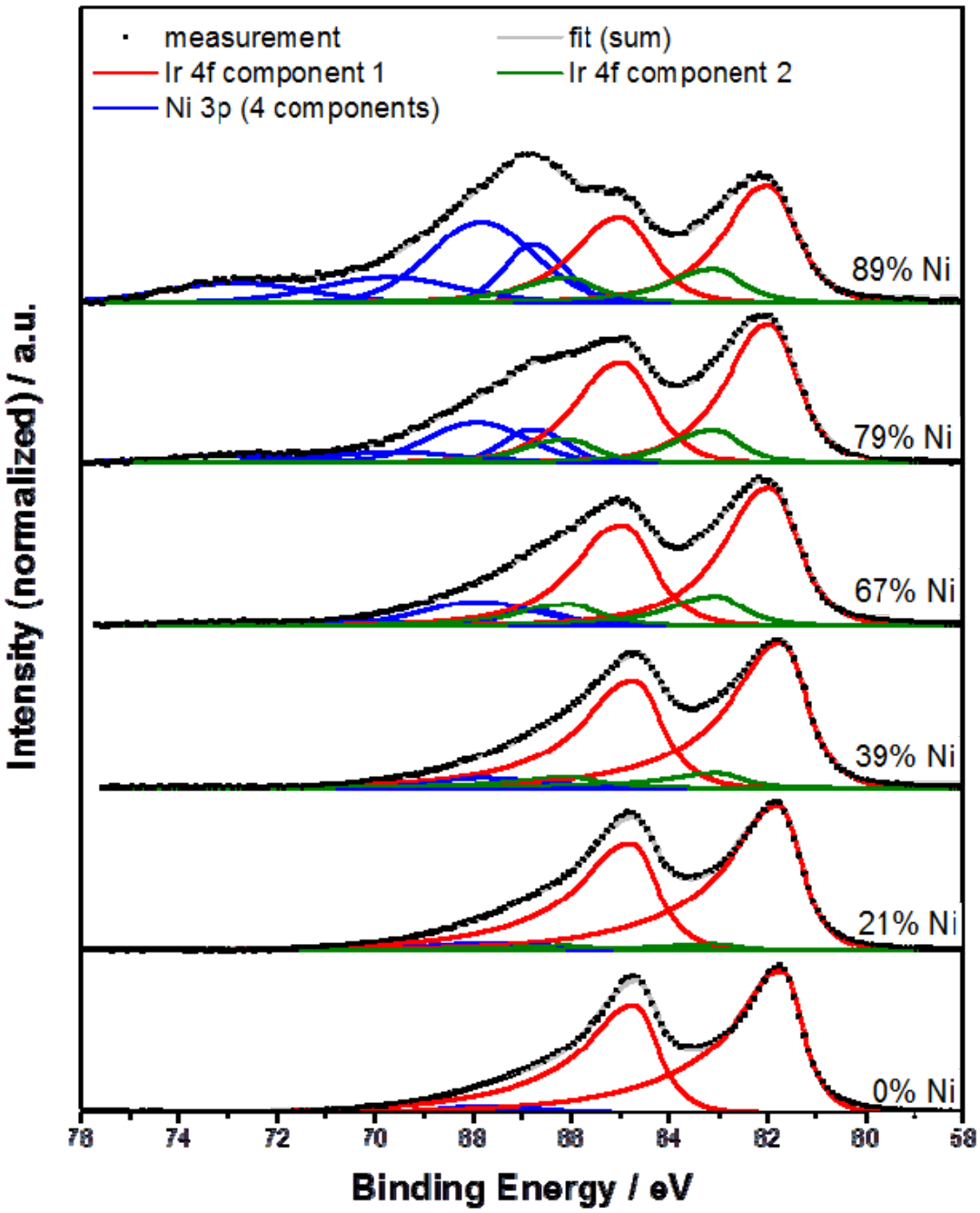

Figure S17: Fitted X-ray photoelectron spectra of the Ir 4f and Ni 3p region of MO-ap.

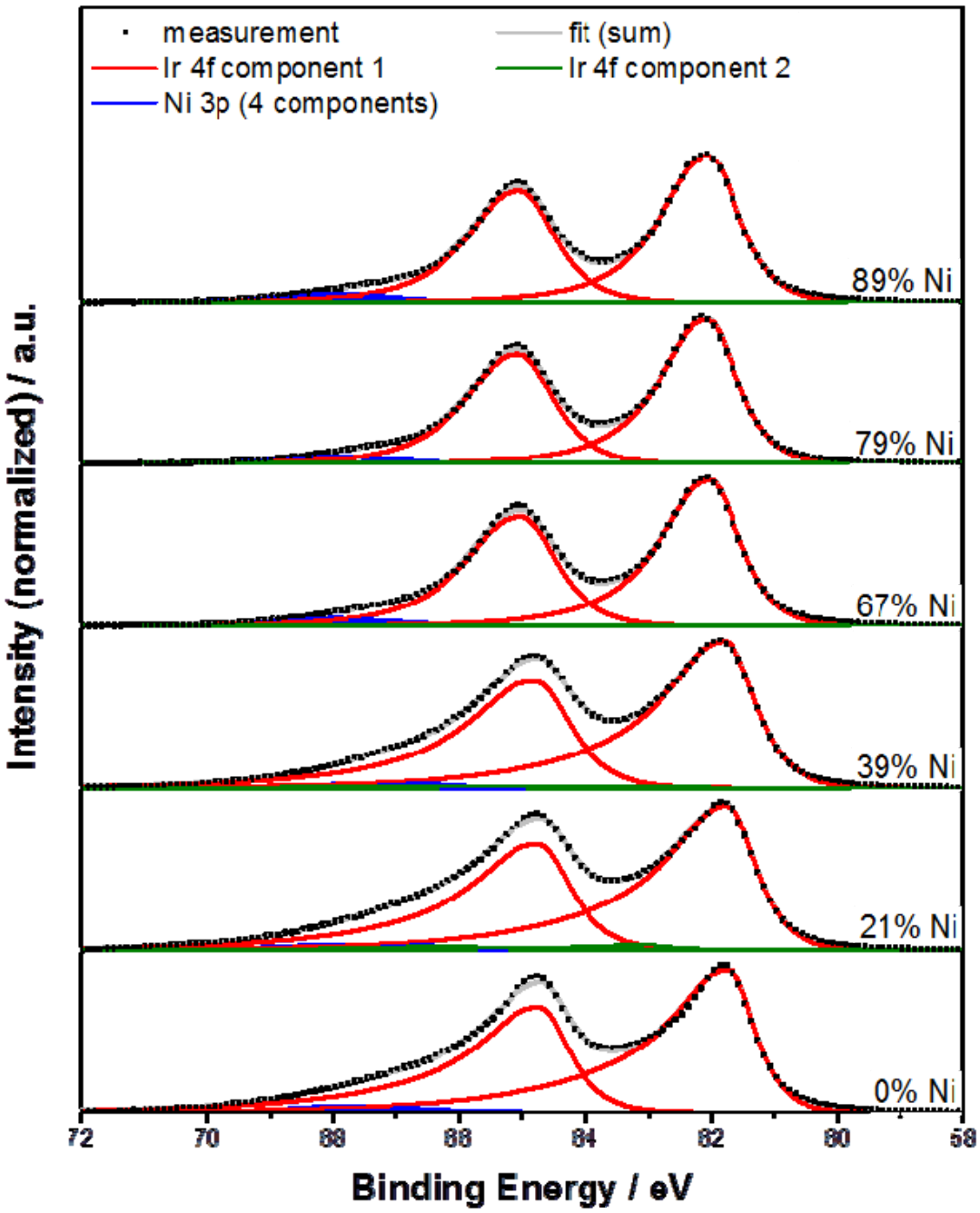

Figure S18: Fitted X-ray photoelectron (XP) spectra of the Ir 4f and Ni 3p region of MO-OER.

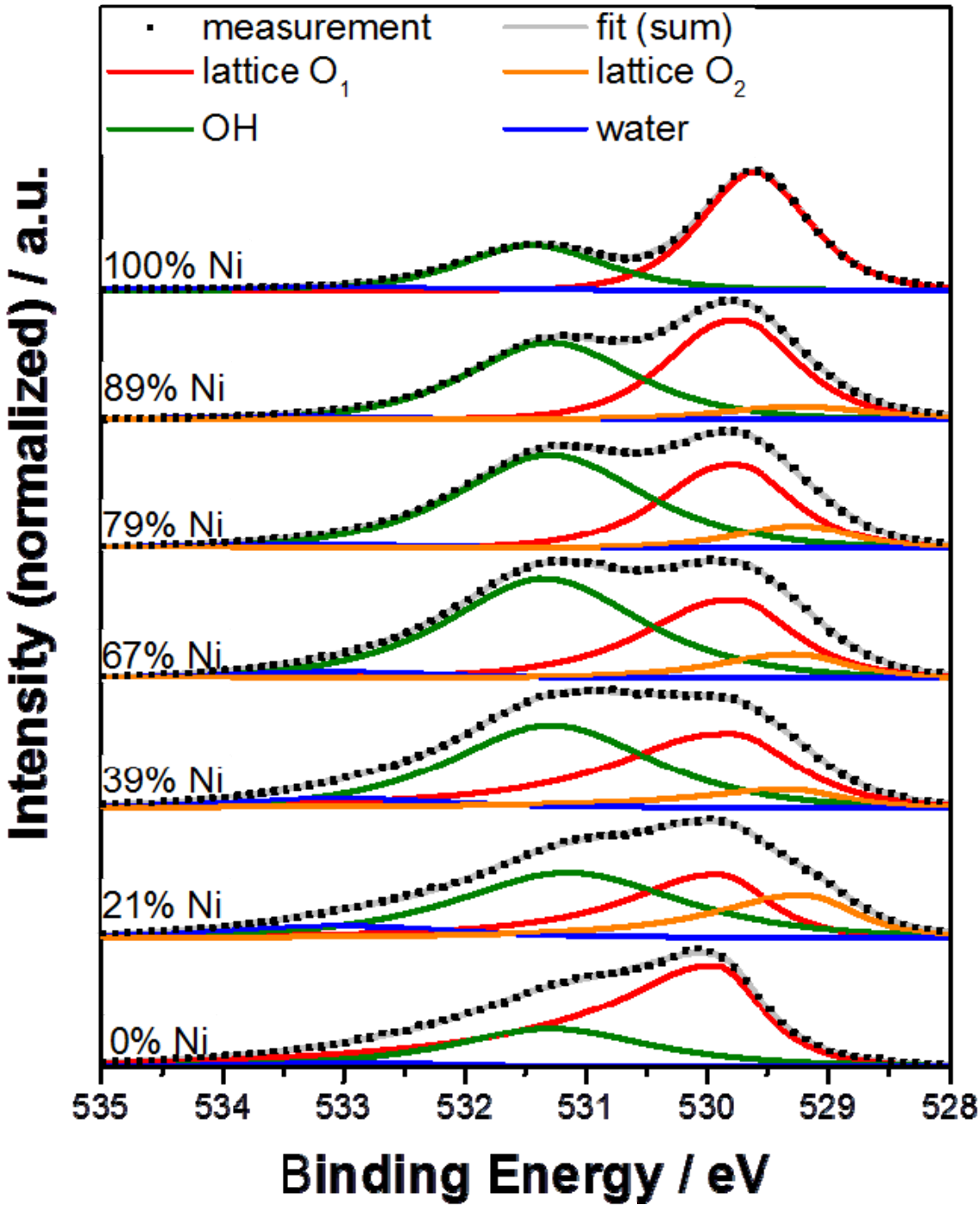

Figure S19: Fitted X-ray photoelectron spectra of the O 1s region of MO-ap.

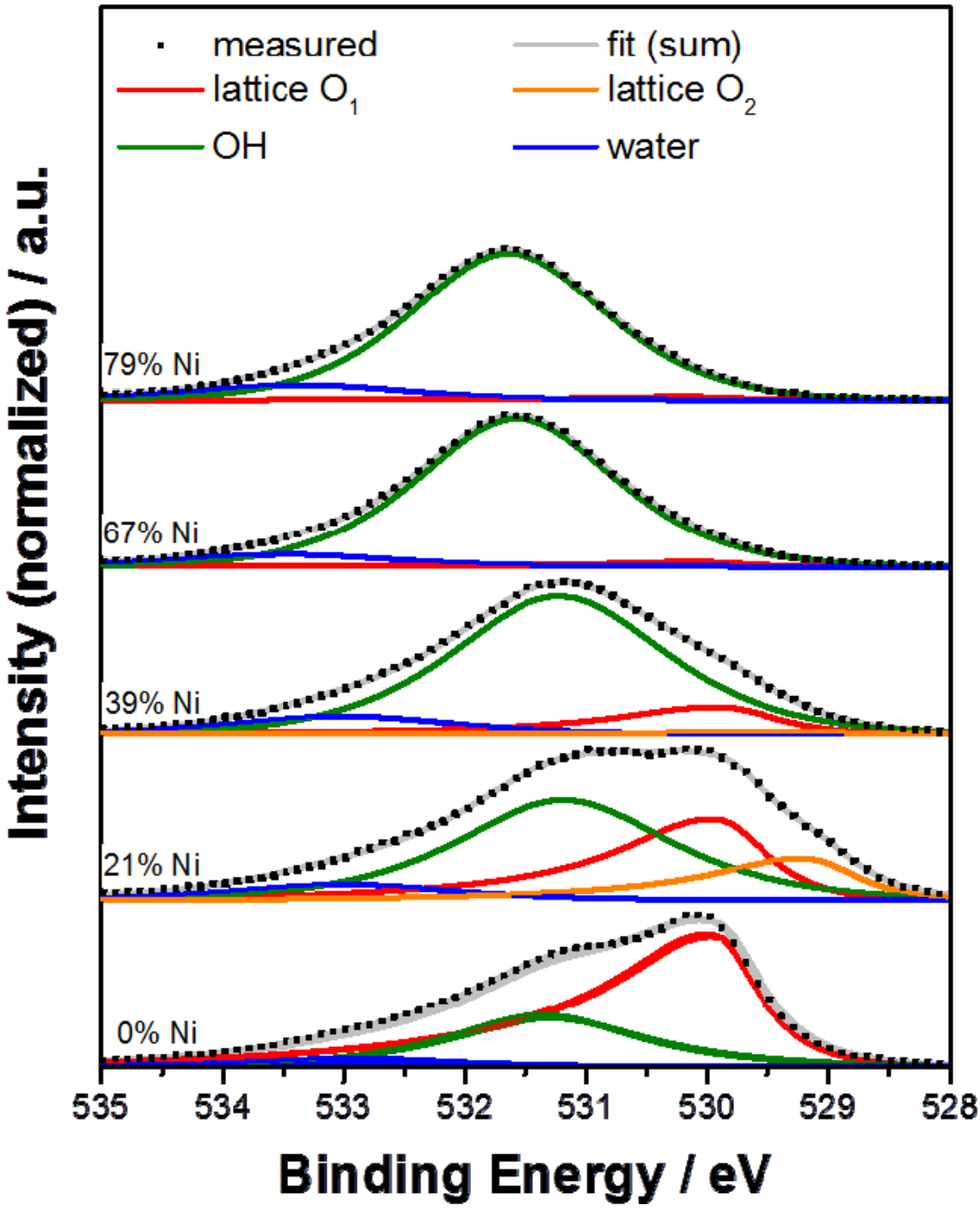

Figure S20: Fitted X-ray photoelectron spectra of the O 1s region of MO-OER.

References

S1 Scofield, J. H. *J. Electron. Spectrosc. Relat. Phenom.* **1976**, *8*, 129.

S2 Tanuma, S.; Powell, C. J.; Penn, D. R. *Surf. Interface Anal.* **1994**, *21*, 165.

S3 Giannozzi, P.; Baroni, S.; Bonini, N.; Calandra, M.; Car, R.; Cavazzoni, C.; Ceresoli, D.; Chiarotti, G. L.; Cococcioni, M.; Dabo, I.; Dal Corso, A.; de Gironcoli, S.; Fabris, S.; Fratesi, G.; Gebauer, R.; Gerstmann, U.; Gougoussis, C.; Kokalj, A.; Lazzeri, M.; Martin-Samos, L.; Marzari, N.; Mauri, F.; Mazzarello, R.; Paolini, S.; Pasquarello, A.; Paulatto, L.; Sbraccia, C.; Scandolo, S.; Sclauzero, G.; Seitsonen, A. P.; Smogunov, A.; Umari, P.; Wentzcovitch, R. M. *J. Phys. Condens. Matter* **2009**, *21*, 395502.

S4 Perdew, J. P.; Burke, K.; Ernzerhof, M. *Phys. Rev. Lett.* **1997**, *78*, 1396.

S5 Marzari, N.; Vanderbilt, D.; De Vita, A.; Payne, M. C. *Phys. Rev. Lett.* **1999**, *82*, 3296.

S6 Cococcioni, M.; de Gironcoli, S. *Phys. Rev. B: Condens. Matter* **2005**, *71*, 035105.

S7 Cheetham, A. K.; Hope, D. A. O. *Phys. Rev. B: Condens. Matter* **1983**, *27*, 6964.

S8 Powell, R. J.; Spicer, W. E. *Phys. Rev. B: Condens. Matter* **1970**, *2*, 2182.

S9 Bengone, O.; Alouani, M.; Blochl, P.; Hugel, J. *Phys. Rev. B: Condens. Matter* **2000**, *62*, 16392.

S10 Pehlke, E.; Scheffler, M. *Phys. Rev. Lett.* **1993**, *71*, 2338.

S11 Gougoussis, C.; Calandra, M.; Seitsonen, A. P.; Mauri, F. *Phys. Rev. B: Condens. Matter* **2009**, *80*, 075102.

S12 Taillefumier, M.; Cabaret, D.; Flank, A. M.; Mauri, F. *Phys. Rev. B: Condens. Matter* **2002**, *66*, 195107.

S13 Menzel, A.; Benzaid, S.; Krause, M. O.; Caldwell, C. D.; Hergenhahn, U.; Bissen, M. *Phys. Rev. A: At. Mol. Opt. Phys.* **1996**, *54*, R991.

S14 Weijs, P. J. W.; Czyzyk, M. T.; Vanacker, J. F.; Speier, W.; Goedkoop, J. B.; Vanleuken, H.; Hendrix, H. J. M.; Degroot, R. A.; Vanderlaan, G.; Buschow, K. H. J.; Wiech, G.; Fuggle, J. C. *Phys. Rev. B: Condens. Matter* **1990**, *41*, 11899.

S15 Kahk, J. M.; Poll, C. G.; Oropeza, F. E.; Ablett, J. M.; Céolin, D.; Rueff, J.-P.; Agrestini, S.; Utsumi, Y.; Tsuei, K. D.; Liao, Y. F.; Borgatti, F.; Panaccione, G.; Regoutz, A.; Egdell, R. G.; Morgan, B. J.; Scanlon, D. O.; Payne, D. J. *Phys. Rev. Lett.* **2014**, *112*, 117601.

S16 Mansour, A. N. *Surf. Sci. Spectra* **1994**, *3*, 211.

S17 Mansour, A. N. *Surf. Sci. Spectra* **1994**, *3*, 231.

S18 Reier, T.; Teschner, D.; Lunkenbein, T.; Bergmann, A.; Selve, S.; Kraehnert, R.; Schlögl, R.; Strasser, P. *J. Electrochem. Soc.* **2014**, *161*, F876.